Tiny *A Priori* Knowledge Solves the Interior Problem in Computed Tomography

Hiroyuki Kudo[1], Matias Courdurier[2], Frédéric Noo[3] and Michel Defrise[4]

[1]Department of Computer Science, University of Tsukuba, Japan
[2]Department of Applied Physics and Applied Mathematics, Columbia University, U.S.A.
[3]Department of Radiology, University of Utah, U.S.A.
[4]Department of Nuclear Medicine, Vrije Universiteit Brussels, Belgium

Abstract. Based on the concept of Differentiated Backprojection (DBP) (Noo *et al* 2004 *Phys.Med.Biol.* **49** 3903-3923, Pan *et al* 2005 *Med.Phys.* **32** 673-684, Defrise *et al* 2006 *Inverse Problems* **22** 1037-1053), this paper shows that the solution to the interior problem in computed tomography is unique if a tiny *a priori* knowledge on the object $f(x, y)$ is available in the form that $f(x, y)$ is known on a small region located inside the region of interest. Furthermore, we advance the uniqueness result to obtain more general uniqueness results which can be applied to a wider class of imaging configurations. We also develop a reconstruction algorithm which can be considered an extension of the DBP-POCS (Projection Onto Convex Sets) method described by Defrise *et al* (2006 *Inverse Problems* **22** 1037-1053), where we not only extend this method to the interior problem but also introduce a new POCS algorithm to reduce computational cost. Finally, we present experimental results which show evidence that the inversion corresponding to each obtained uniqueness result is stable.

Keywords: Tomography, Image reconstruction, Interior problem, Truncation, Differentiated backprojection, Hilbert transform, POCS

Submitted Journal: Physics in Medicine and Biology

Corresponding Author:
Dr. Hiroyuki Kudo
Department of Computer Science
Graduate School of Systems and Information Engineering
University of Tsukuba
Tennoudai 1-1-1, Tsukuba 305-8573, Japan
Tel: 81-29-853-5516, Fax: 81-29-853-5516
E-mail: kudo@cs.tsukuba.ac.jp

1. Introduction

This paper deals with 2-D region-of-interest (ROI) reconstruction from truncated projection data in Computed Tomography (CT) (Lewitt 1979, Ogawa *et al* 1984, Natterer 1986, Louis and Rieder 1989, Maass 1992, Olson and DeStafano 1994, Ohnesorge *et al* 2000, Clackdoyle *et al* 2004, Noo *et al* 2004, Zhuang *et al* 2004, Zou and Pan 2004, Pack *et al* 2005, Pan *et al* 2005, Ye *et al* 2005, Zou *et al* 2005, Defrise *et al* 2006, Kudo 2006, Yu *et al* 2006, Courdurier 2007a, 2007b, Kudo *et al* 2007, Ye *et al* 2007, Zhang and Zeng 2007). This problem aims at reconstructing an object on a ROI (smaller than the whole object) from the limited set of projection data which corresponds to all lines passing through the ROI. For a long time, due to the non-local nature of Filtered Backprojection (FBP) method, it had been believed that the solution to this problem is not unique. However, the concept of Differentiated Backprojection (DBP) introduced by Noo *et al* (2004) and Pan *et al* (2005) clarified that this problem can be exactly solved for imaging configurations satisfying some geometrical condition. Furthermore, very recently, Defrise *et al* (2006) showed that the geometrical condition which assures a unique solution of the ROI reconstruction can be significantly relaxed. Their approach is also based on the DBP concept. It is also known that the DBP concept can be generalized to cone-beam tomography and other imaging geometries in a natural way (Rullgard 2004, Zhuang *et al* 2004, Zou and Pan 2004, Pack *et al* 2005, Ye *et al* 2005, Zou *et al* 2005, Yu *et al* 2006). Furthermore, it became clear that Gelfand and Graev (1991) had already developed the same method before the community of image reconstruction discovered this innovative idea. Clackdoyle *et al* (2004) presented an alternative approach to enable exact reconstruction of the ROI from the truncated projection data. An important problem which has not been investigated yet using the DBP concept is the so-called interior problem shown in figure 1(a). In this problem, the ROI S is wholly contained inside the object $f(x, y)$ and we can measure the limited set of projection data which corresponds to all lines passing through S. Long time ago, Natterer (1986) had already proved that the solution to this problem is not unique even if we know exact information on the object support. Though the interior problem has been a topic in image reconstruction for a long time (Lewitt 1979, Ogawa *et al* 1984, Natterer 1986, Louis and Rieder 1989, Maass 1992, Olson and DeStafano 1994, Ohnesorge *et al* 2000, Zhang and Zeng 2007), to our knowledge, no one have investigated this problem with the DBP concept.

The purpose of this paper is as follows. First, we show that the solution to the interior problem is unique if a tiny *a priori* knowledge on the object $f(x, y)$ is available in the form that $f(x, y)$ is known on a small region B located inside S. The proof is based on the DBP approach similar to that by Defrise *et al* (2006), *i.e.* we reduce the image reconstruction to the inversion of 1-D Hilbert transform along a set of straight lines by using the DBP and then show uniqueness of the Hilbert inversion. Second, we advance the uniqueness result for the interior problem to obtain more general uniqueness results which can be applied to a wider class of imaging configurations. Third, we develop

a reconstruction algorithm which can be considered an extension of the DBP-POCS (Projection Onto Convex Sets) method described by Defrise *et al* (2006), where we not only extend this method to the interior problem but also introduce a new POCS algorithm to reduce computational cost of the DBP-POCS method. Finally, we present experimental results which show evidence that the inversion corresponding to each obtained uniqueness result is stable.

Apart from the theoretical contribution, we note that the results in this paper possess an important application which is to reduce patient dose in CT imaging. In many situations of CT imaging, physicians are interested only in a relatively small ROI containing heart, breast, or some specific organ. Current CT systems are unable to properly handle the interior problem and, therefore, in such a case, they require exposing x-rays to the whole section containing the ROI. Our exact approaches for the interior problem have the potential to allow decreasing the radiation exposure outside the ROI while keeping a good signal-to-noise ratio within the ROI. Other applications would be to reduce necessary detector size and to achieve higher image magnification factor in the ROI imaging.

We note that earlier versions of this work have been already disclosed in some seminars and conferences since November, 2006 (Kudo 2006, Courdurier 2007a, 2007b, Kudo *et al* 2007). We note also that, very recently, Ye *et al* (2007) published a paper related to the topic of this paper, the results of which partly overlap with our results. The details of this overlap are clarified at the end of this paper.

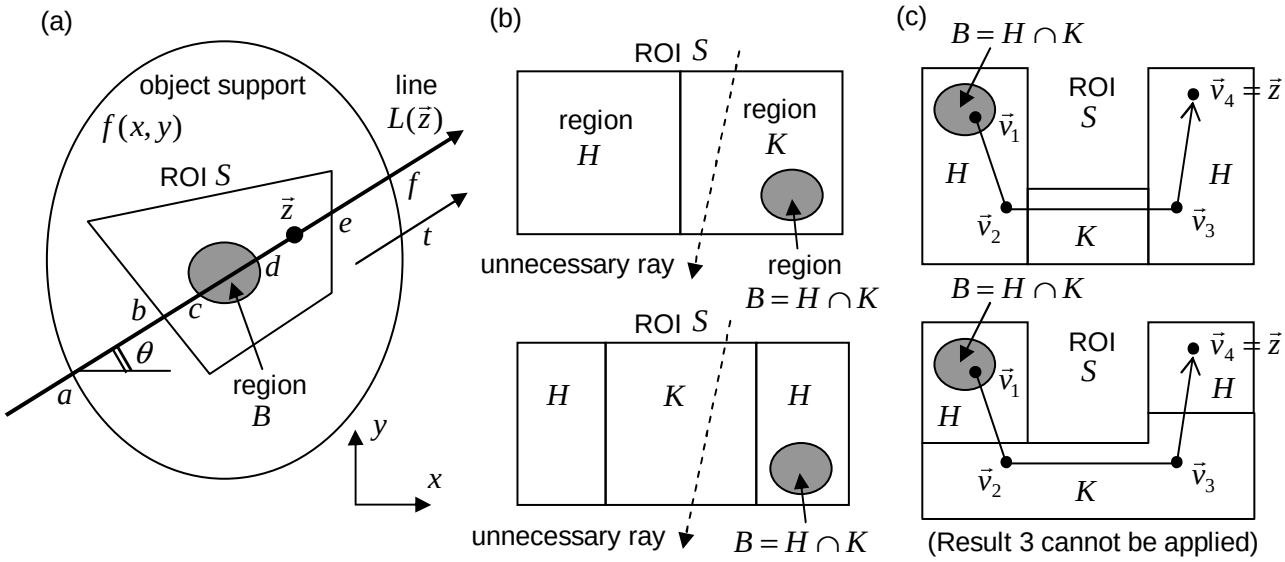

Figure 1. Various imaging configurations in the interior problem which correspond to (a) Result 1, (b) Result 2, and (c) Result 3.

2. Uniqueness Results

2.1. Uniqueness for the Interior Problem

This section describes the main uniqueness result for the interior problem under the assumption that *a priori* knowledge on the object is available in addition to measured projection data. Let $f(x, y)$ denote a 2-D object. We assume that $f(x, y)$ is a continuous function having a finite support. Let $p(r, \phi)$ denote parallel-beam projection data expressed as

$$p(r, \phi) = \int_{-\infty}^{\infty} ds \; f(r\cos\phi - s\sin\phi, r\sin\phi + s\cos\phi), \tag{1}$$

where r is the radial variable and ϕ is the angle. We consider the interior problem shown in figure 1(a). In this problem, we would like to reconstruct $f(x, y)$ on a ROI S wholly contained inside the object. We assume that S is a convex set‡. We can measure the limited set of projection data which corresponds to all lines passing through S. The aim in this section is to show that this problem can be exactly solved if a tiny *a priori* knowledge on the object $f(x, y)$ is available in the form that $f(x, y)$ is known on a small region B (having non-zero measure) located inside S (figure 1(a)). For simplicity, we assume that B is also a convex set.

The proof is based on the DBP approach similar to that by Defrise *et al* (2006), *i.e.* we reduce the image reconstruction to the inversion of 1-D Hilbert transform along a set of straight lines by using the DBP and then show uniqueness of the Hilbert inversion. Let us consider a particular point $\vec{z} = (x_0, y_0)$ to be reconstructed located inside S (and outside B). Then, we take a (directed) straight line $L(\vec{z})$ passing through both $\vec{z}$ and B (such $L(\vec{z})$ always exists). We apply the DBP to the projection data $p(r, \phi)$ along the line $L(\vec{z})$ where the angle θ in the sign reversal factor $\mathrm{sgn}(\cdot)$ is set to the tilt angle of $L(\vec{z})$ (figure 1(a)) (Noo *et al* 2004, Pan *et al* 2005, Defrise *et al* 2006):

$$g_\theta(x, y) = \frac{-1}{2\pi} \int_0^{\pi} d\phi \; \frac{\partial}{\partial r} p(r, \phi)\Big|_{r=x\cos\phi+y\sin\phi} \mathrm{sgn}(\cos(\phi - \theta)) \tag{2}$$

Then, the relation between the outcome $g_\theta(x, y)$ and the object $f(x, y)$ is as follows (Noo *et al* 2004, Pan *et al* 2005, Defrise *et al* 2006). We define the 1-D coordinate t along the line $L(\vec{z})$ such that the direction of the t-axis coincides with that of $L(\vec{z})$. We represent $f(x, y), g_\theta(x, y)$ restricted to $L(\vec{z})$ by 1-D functions $f(t), g(t)$, respectively. Take the points (a, b, c, d, e, f) on the t coordinate as shown in figure 1(a), *i.e.* $a < b < c < d < e < f$, the interval $a < t < f$ corresponds to the object support, the interval $b < t < e$ corresponds to the ROI S, and the interval $c < t < d$ corresponds to the region B. Then, the Hilbert transform of $f(t)$ equals to $g(t)$ as

$$g(t) = \frac{1}{\pi} \; \mathrm{p.v.} \int_a^f ds \; \frac{1}{t - s} f(s) \; (b < t < e), \tag{3}$$

‡ The convexity assumption of the ROI S is natural because, for any limited set of the projection data $p(r, \phi)$, the maximum region on which the backprojection from a 180° angular range can be computed is necessarily a convex set or a union of disjoint convex sets.

where p.v. denotes Cauchy's principal value of the integral. The significance of this result is that the reconstruction of $f(x, y)$ along the line $L(\vec{z})$ can be reduced to the inversion of Hilbert transform expressed by equation (3). We make the following remark on the interval on which $g(t)$ can be accessed in equation (3). Since $p(r, \phi)$ is measured for all lines passing through S, $g(t)$ can be accessed on the interval $b < t < e$ using the DBP of equation (2). However, outside $b < t < e$, $g(t)$ cannot be accessed because $p(r, \phi)$ is not measured over the 180° angular range required to compute the DBP. From this fact, in the interior problem, the measured interval of $g(t)$ in equation (3) is smaller than the support of $f(t)$. In this sense, the Hilbert transform expressed by equation (3) should be called the truncated Hilbert transform.

If $g(t)$ is measured on a larger interval $a < t < f$, we can use well-known Tricomi's inversion formula of the finite Hilbert transform to invert equation (3) (Tricomi 1957, Gakhov 1966, Pandy 1995):

$$\begin{aligned} f(t) &= \frac{1}{W(t)}(C_{af} + \frac{1}{\pi}\ \text{p.v.} \int_a^f ds\ \frac{1}{s-t} g(s)W(s))\ (a < t < f) \\ W(t) &= \sqrt{(f-t)(t-a)} \\ C_{af} &= \frac{1}{\pi}\int_a^f dt\ f(t), \end{aligned} \tag{4}$$

where we note that the constant C_{af} is the projection data $p(r, \phi)$ measured along the line $L(\vec{z})$ (divided by π), which is known. However, given $g(t)$ on the limited interval $b < t < e$, the integral equation of equation (3) does not admit a unique solution for $f(t)$ on any interval. Therefore, we use the *a priori* knowledge that $f(t)$ is known on the interval $c < t < d$. We assume that we know *a priori* that $f(t) = f^{(p)}(t)$ on $c < t < d$ where $f^{(p)}(t)$ is a known function. In this case, the problem can be formulated as solving the integral equation constrained on the solution $f(t)$:

$$\begin{aligned} &g(t) = \frac{1}{\pi}\ \text{p.v.} \int_a^f ds\ \frac{1}{t-s} f(s)\ (b < t < e) \\ &\text{subject to } f(t) = f^{(p)}(t) \text{ for } c < t < d \end{aligned} \tag{5}$$

The inversion of equation (5) for $f(t)$ has essentially the same structure as that investigated by Defrise *et al* (2006). However, there exist the following two differences between the both. The first difference lies in the location of the interval on which we know $f(t)$, *i.e.* in Defrise *et al* (2006) $f(t)$ must be known on a segment containing a boundary of the object support, but now we only need to know $f(t)$ on the internal segment $c < t < d$ in equation (5). The second difference lies in the form of known function $f^{(p)}(t)$, *i.e.* $f^{(p)}(t) = 0$ in Defrise *et al* (2006) but $f^{(p)}(t)$ is a general function in equation (5). Taking these differences into account, we followed the same approach as that in Defrise *et al* (2006) to show that $f(t)$ is uniquely determined on the interval $b < t < e$ (containing $\vec{z}$). We leave the proof for this part to Appendix A. Since the above explanation can be applied to any point $\vec{z}$ located inside S, we immediately obtain the following result.

[Result 1] Let S be a convex ROI (wholly contained inside the object). Assume that we can measure projection data $p(r, \phi)$ for all lines passing through S. Assume that we know $f(x, y)$ *a priori* on a region B (having non-zero measure) located inside S. Then, $f(x, y)$ is uniquely determined on S. ∎

A surprising fact is that B can be an arbitrarily small region having non-zero measure. Therefore, the *a priori* knowledge to assure the uniqueness can be tiny. Though we think that stability of the inversion becomes worse if the region B diminishes closer to a single point, the simulation results shown later demonstrate that a relatively small region B works well in practice.

2.2. Further Extensions

In this section, we extend the uniqueness result in section 2.1 to a wider class of imaging configurations. The main limitation of Result 1 is that we need to measure the projection data $p(r, \phi)$ for all lines passing through the ROI S. This seems not to be an absolute requirement when a strong *a priori* knowledge on the object $f(x, y)$ is available. For example, if we know $f(x, y)$ on a larger region K inside S as shown in figure 1(b), the necessary amount of projection data would be significantly reduced. Unfortunately, Result 1 is not valid to demonstrate such possibility. Hereafter, along this direction, we first describe a new uniqueness result (Result 2) and then show its proof.

[Result 2] Let S be a convex ROI (wholly contained inside the object). Let H be a subset of S on which we can access the 1-D Hilbert transform $g_\theta(x, y)$ using the DBP. Let K be a subset of S on which the object $f(x, y)$ is known *a priori*. Then, $f(x, y)$ is uniquely determined on S if the following two conditions are satisfied.
(1) The subsets H and K satisfy $H \cup K = S$, *i.e.* we know either the Hilbert transform g_θ or the object f itself on every point inside S.
(2) Let $B = H \cap K$, *i.e.* B is the subset of S on which we know both the Hilbert transform g_θ and the object f. Then, B is a non-empty set having non-zero measure. ∎

To avoid a confusion in the used symbols, we again note that the symbol H ("Hilbert") denotes the region on which the Hilbert transform g_θ is accessible, the symbol K ("Known") denotes the region on which the object f is known, and the symbol B ("Both") denotes the region on which both g_θ and f are known. We also note again that, for any limited set of the projection data $p(r, \phi)$, the maximum region H on which the DBP can be computed is necessarily a convex set or a union of disjoint convex sets. In figure 1(b), we show two imaging configurations for which Result 2 can be applied to show the uniqueness but Result 1 is not valid (of course, these ROIs S are wholly contained inside the object, which is not shown in the figure). In the top example, the rectangular ROI S is a union of two squares (left and right). We can measure $p(r, \phi)$ only for all lines passing through the left square H, *i.e.* the Hilbert transform $g_\theta(x, y)$ is accessed using the DBP on H. We know $f(x, y)$ on the right square K. In addition, there exists a small region B on which we know both $g_\theta(x, y)$ and $f(x, y)$. Notice that,

in this case, rays not passing through H need not be measured (recall that H always contains B from the definition). These simple examples would be enough to convince readers that Result 2 is stronger than Result 1, in the sense that it clearly succeeds in reducing the necessary amount of projection data when the subset K, on which $f(x, y)$ is known *a priori*, is large.

We show the proof of Result 2 below. For each point $\vec{z}$ to be reconstructed located inside S (and outside B), we take a (directed) straight line $L(\vec{z})$ passing through both $\vec{z}$ and B (such $L(\vec{z})$ always exists), and apply the DBP along $L(\vec{z})$. Then, from the definition of the symbols (K, H, B), the DBP of equation (2) allows us to access the 1-D Hilbert transform $g_\theta(x, y)$ on the region H but not on the region $K \setminus B$ (recall that both H and K always contain B). Therefore, in the same way as in equation (5), the integral equation (constrained on the solution $f(t)$) to be inverted takes the following form:

$$\begin{aligned} &g(t) = \frac{1}{\pi}\ \text{p.v.} \int_\Lambda ds\ \frac{1}{t-s} f(s)\ (t \in \Lambda_H) \\ &\text{subject to } f(t) = f^{(p)}(t) \text{ for } t \in \Lambda_K, \end{aligned} \tag{6}$$

where Λ, Λ_H, and Λ_K denote the intervals (or unions of disjoint intervals) on the t coordinate axis corresponding to the object support, the subset H, and the subset K, respectively. On the other hand, from the two conditions (1),(2) of Result 2, we know that

$$\Lambda_H \cup \Lambda_K = \Lambda_S,\ \Lambda_B = \Lambda_H \cap \Lambda_K \neq \{\phi\}, \tag{7}$$

where Λ_S and Λ_B are the intervals on the t coordinate corresponding to the ROI S and the subset B, respectively. Clearly, equation (6) with equation (7) can be considered a generalization of equation (5). The analysis of equation (6) under equation (7) along the similar line to Defrise *et al* (2006) clarifies that $f(t)$ is uniquely determined on the interval Λ_S (containing $\vec{z}$). We leave the proof for this part to Appendix B. Since the above explanation can be applied to every point located inside S, we immediately obtain Result 2.

The final goal of this section is to remove the requirement that the ROI S must be convex in Result 2. A non-convex (but pathwise-connected) ROI such as those in figure 1(c) might appear in some imaging situations§. We found that uniqueness of the ROI reconstruction still holds even for the non-convex ROI if an additional geometrical condition on the configuration of the subsets (K, H, B) is satisfied. We describe the result together with the proof as follows.

[Result 3] Let S be a pathwise-connected ROI (wholly contained inside the object) where S can be non-convex. Let us define the subsets (K, H, B) in the same way as in Result

§ In section 2.1, we assumed that the ROI S is a convex set because of the fact that, for any limited set of the projection data $p(r, \phi)$, the maximum region H on which the DBP can be computed is a convex set or a union of disjoint convex sets. However, when the *a priori* knowledge of $f(x, y)$ on the region K is available, it is natural to assume that the ROI S is a non-convex set. This is because $S = H \cup K$ can be a non-convex set by the facts that a union of multiple convex sets can create a non-convex set and that K itself can be non-convex.

2. Then, $f(x, y)$ is uniquely determined on S if the following condition (3), in addition to the two conditions (1),(2) of Result 2, is satisfied.
(3) For every point $\vec{z}$ inside S (and outside B), as shown in the top case of figure 1(c), there exists a polygonal path constructed by vertices $\vec{v}_1, \vec{v}_2, \ldots, \vec{v}_N$ ($N \geq 3$ is an arbitrary positive integer) which starts from a point inside the subset B (*i.e.* $\vec{v}_1 \in B$) and reaches to the point $\vec{z}$ (*i.e.* $\vec{v}_N = \vec{z}$) such that (a) the path is contained inside S and (b) all the intermediate vertex points $\vec{v}_2, \vec{v}_3, \ldots, \vec{v}_{N-1}$ are located inside the subset H (recall that H always contains B). ∎

As described above, to apply Result 3, for any $\vec{z} \in S$, all the intermediate vertex points $\vec{v}_2, \vec{v}_3, \ldots, \vec{v}_{N-1}$ of some polygonal path must be able to be located inside the subset H. This is an additional restriction on the configuration of the subsets (K, H, B) when the ROI S is non-convex. For example, the top example in figure 1(c) satisfies this condition, but the bottom example does not because, to draw a polygonal path for some $\vec{z} \in S$ in this example, at least one of the intermediate vertex points $\vec{v}_2, \vec{v}_3, \ldots, \vec{v}_{N-1}$ must be taken inside the subset $K \setminus B$ (not H). On the other hand, when the ROI S is convex, it is easy to see that the condition (3) of Result 3 is automatically satisfied by taking the polygonal path with $N = 3$ such that $v_1 \in B, v_2 \in B, v_3 = \vec{z}$ for any $\vec{z} \in S$ (figure 2(a)). Consequently, Result 3 coincides with Result 2 for a convex ROI. It is still an open problem whether this additional condition can be dropped or not for the non-convex ROI.

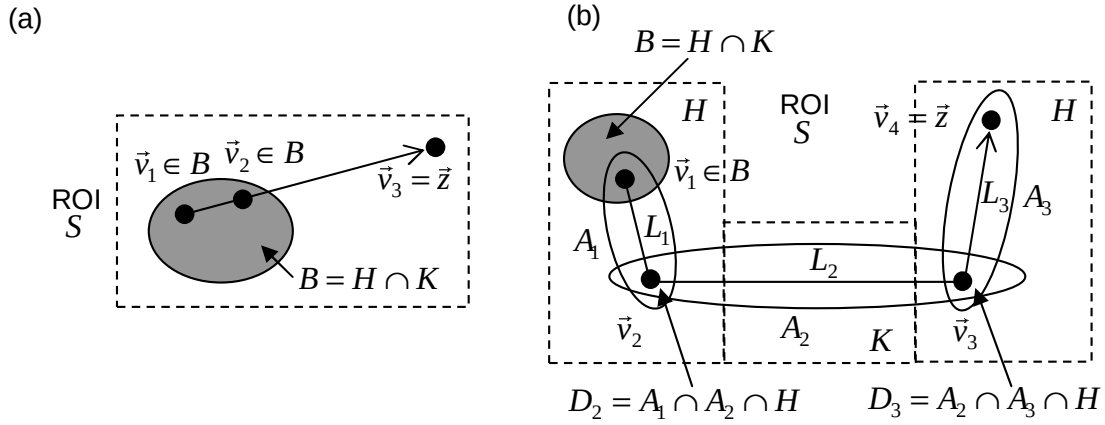

Figure 2. (a) The polygonal path with $N = 3$ satisfying the additional condition (3) of Result 3 when the ROI S is convex. (b) The illustration for the proof of Result 3.

The proof of Result 3 is as follows. See figure 2(b) for the illustration concerning this proof. For each $\vec{z} \in S$, we consider the polygonal path $\vec{v}_1, \vec{v}_2, \ldots, \vec{v}_N$ with $N \geq 3$ satisfying the condition (3) of Result 3. For $i = 1, 2, \ldots, N-1$, we denote the line segment connecting the successive two vertices $\vec{v}_i, \vec{v}_{i+1}$ by L_i. For each L_i, we can always take a convex set A_i such that $A_i \supset L_i$ and $A_i \subset S$, *i.e.* A_i is the region which contains L_i inside and is contained inside the ROI S. Then, it is clear that $D_i = A_{i-1} \cap A_i \cap H$ $(i = 2, 3, \ldots, N-1)$ is a non-empty set having non-zero measure because $\vec{v}_2, \vec{v}_3, \ldots, \vec{v}_{N-1}$ are located inside the subset H. We are ready to prove Result

3. First, applying Result 2 to the set A_1, $f(x,y)$ is uniquely determined on A_1 because A_1 contains a part of B. Therefore, we know both $f(x,y)$ and $g_\theta(x,y)$ on D_2. Next, applying Result 2 again to the set A_2 by taking the set D_2 as the set B, $f(x,y)$ is uniquely determined on A_2. Therefore, we know both $f(x,y)$ and $g_\theta(x,y)$ on D_3. This process is repeated through $A_3, A_4, \ldots, A_{N-2}$ to A_{N-1} so that we can show that $f(x,y)$ is unique on A_{N-1}. Since A_{N-1} contains $\vec{z}$, $f(x,y)$ is uniquely determined on $\vec{z}$. The proof is completed because the above explanation can be applied to every point $\vec{z} \in S$.

As colloraries of Result 2 and Result 3, we also obtain the following results which can handle more general imaging configurations including, in particular, the case where the ROI S is a union of disjoint sets.

[Result 4] Let S be a ROI which is a union of disjoint sub-ROIs $S_1, S_2, \ldots, S_I$ (wholly contained inside the object), *i.e.* $S = \cup_{i=1}^{I} S_i$ and $S_i \cap S_j = \{\phi\}$ for all $i \neq j$. Assume that each sub-ROI S_i is pathwise-connected but can be non-convex. Then, if every S_i $(i = 1, 2, \ldots, I)$ satisfies the conditions for uniqueness described in Result 2 or Result 3, $f(x,y)$ is uniquely determined on S. ∎

[Result 5] Let S be a ROI (wholly contained inside the object) where S can be non-convex and can be a union of disjoint sub-ROIs. Let S' be a subset of S such that $S' \cup K = S$, *i.e.* the union of S' and K covers the whole ROI S. Then, if S' satisfies the conditions for uniqueness in Result 2, Result 3, or Result 4, $f(x,y)$ is uniquely determined on S. ∎

3. Reconstruction Algorithms

3.1. Overall Algorithm Structure

For all of the five results described in section 2, we do not have analytical inversion formulae similarly to the case dealt with by Defrise *et al* (2006). Therefore, we use the DBP-POCS method described in Defrise *et al* (2006), modified to enforce the *a priori* knowledge on the object $f(x,y)$ as a constraint during the Hilbert inversion. This algorithm first performs the DBP of equation (2) along a set of straight lines (called the Hilbert lines) passing through the region B to create the 1-D (truncated) Hilbert transform of $f(x,y)$ along each Hilbert line. Then, the Hilbert transform is inverted by using the iterative POCS algorithm developed for signal and image recovery problems (Youla and Webb 1982, Combettes 1993, Stark and Yang 1998). The overall structure of the algorithm corresponding to Result 2 (containing Result 1 as a special case) in section 2 is summarized as follows.

[Step 1] (Define the Hilbert lines) Given a configuration of the subsets (K, H, B), define a set of the Hilbert lines $L(u); u \in U$ (u is the 1-D parameter to parameterize a set of the lines), such that (a) every Hilbert line $L(u)$ passes through the region B and (b) every point $\vec{z}$ inside the ROI S lies on a Hilbert line $L(u(\vec{z}))$. We denote the relation between the (x,y) coordinates and the (u,t) coordinates by $u(x,y), t(x,y)$, where t is the coordinate along each Hilbert line $L(u(\vec{z}))$. In figure 3, we show two typical examples

on how to choose the set of the Hilbert lines. ∎
[Step 2] (DBP) Along each Hilbert line $L(u)$, we compute the DBP by equation (2) to obtain the 1-D (truncated) Hilbert transform $g_\theta(x, y)$ on the subset H containing B (not for the subset $K \setminus B$). The angle θ in the sign reversal factor $\mathrm{sgn}(\cdot)$ of equation (2) must be set to the tilt angle of each Hilbert line $L(u)$. ∎
[Step 3] (Hilbert inversion by POCS) Along each Hilbert line $L(u)$, we invert the (truncated) Hilbert transform (solve equation (6)) by using the POCS algorithm to obtain a function $f_u(t)$ which is same as $f(x, y)$ but is represented on the (u, t) coordinates. This step is explained in detail in sections 3.2. ∎
[Step 4] (Coordinate transform) From the relation $f(x, y) = f_{u(x,y)}(t(x, y))$, we obtain $f(x, y)$. In the special case where $L(u); u \in U$ is well-defined (such as the example in figure 3(a)), this step is unnecessary. ∎

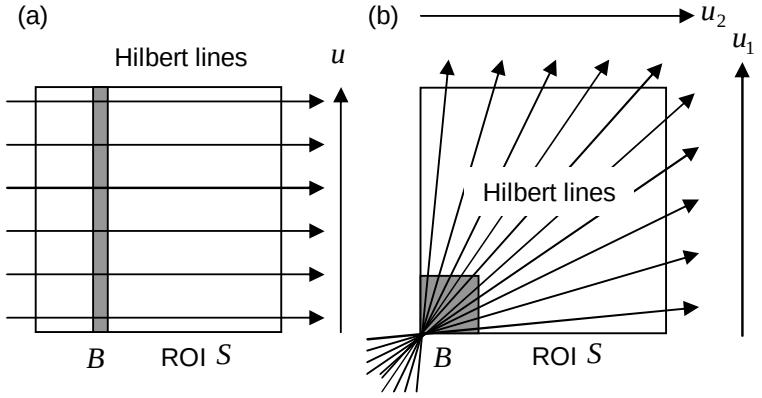

Figure 3. Two typical choices of a set of the Hilbert lines.

3.2. Hilbert Inversion by POCS

This section proposes two different POCS algorithms for the Hilbert inversion which appears in Step 3. The problem here is to solve the integral equation given by equation (6) along each Hilbert line $L(u)$. We note that equation (5) corresponding to Result 1 is a special case of equation (6). The first POCS algorithm called POCS-1 is a direct extension of the method described by Defrise *et al* (2006). Let $(Hf)(t)$ denote the Hilbert transform of $f(t) \in L^2(\mathbb{R})$. Then, this method aims at finding $f(t) \in L^2(\mathbb{R})$ which belongs to the intersection of the following five convex sets:

$$
\begin{aligned}
C_1 &= \{f \in L^2(\mathbb{R}) \mid (Hf)(t) = g(t) \text{ for } t \in \Lambda_H\} \\
C_2 &= \{f \in L^2(\mathbb{R}) \mid f(t) = 0 \text{ for } t \notin \Lambda\} \\
C_3 &= \{f \in L^2(\mathbb{R}) \mid f(t) = f^{(p)}(t) \text{ for } t \in \Lambda_K\} \\
C_4 &= \{f \in L^2(\mathbb{R}) \mid \int_{\Lambda \setminus \Lambda_K} dt\ f(t) = C_\Lambda^{(p)}\} \\
C_\Lambda^{(p)} &= \pi C_\Lambda - \int_{\Lambda_K} dt\ f^{(p)}(t),\ C_\Lambda = \frac{1}{\pi} \int_\Lambda dt\ f^{(o)}(t)
\end{aligned}
$$

$$C_5 = \{f \in L^2(\mathbb{R}) \mid f(t) \geq 0 \text{ for } t \in \mathbb{R}\}, \tag{8}$$

where $f^{(o)}(t)$ used in the constant C_Λ denotes the true object $f^{(o)}(x, y)$ restricted to each Hilbert line $L(u)$. We note that C_Λ is known, because it is equal to the projection data of $f^{(o)}(x, y)$ along each Hilbert line $L(u)$ (divided by π) and this quantity is measured. The iteration formula to find $f(t)$ which belongs to the intersection $C = \cap_{i=1}^5 C_i$ is given by

$$f^{(0)} : \text{ arbitrary}, \quad f^{(k+1)} = P_5 P_4 P_3 P_2 P_1 f^{(k)}, \tag{9}$$

where k denotes the iteration number, and P_i denotes the projection operator onto the set C_i (Youla and Webb 1982, Combettes 1993, Stark and Yang 1998). The detailed form of P_i for each i is as follows. P_2, P_3, P_5 have straightforward expressions (omitted here), and P_1, P_4 are expressed as

$$\begin{aligned}
&(P_1 f)(t) = (H^{-1} M H f)(t) \\
&(Hf)(t) = \frac{1}{\pi} \text{ p.v.} \int_{-\infty}^{\infty} ds \ \frac{1}{t-s} f(s) \\
&(H^{-1} h)(t) = \frac{1}{\pi} \text{ p.v.} \int_{-\infty}^{\infty} ds \ \frac{1}{s-t} h(s) \\
&(Mh)(t) = \begin{cases} g(t) & (t \in \Lambda_H) \\ h(t) & (t \notin \Lambda_H) \end{cases}
\end{aligned} \tag{10}$$

$$(P_4 f)(t) = \begin{cases} f(t) + \dfrac{C_\Lambda^{(p)} - \displaystyle\int_{\Lambda \setminus \Lambda_K} dt' \ f(t')}{\displaystyle\int_{\Lambda \setminus \Lambda_K} dt'} & (t \in \Lambda \setminus \Lambda_K). \\ f(t) \quad (t \notin \Lambda \setminus \Lambda_K) \end{cases} \tag{11}$$

We note that P_1 is computed by taking the Hilbert transform H followed by enforcing the constraint $(Hf)(t) = g(t)$ for $t \in \Lambda_H$ and then taking the inverse Hilbert transform H^{-1}. In this formulation in the $L^2(\mathbb{R})$ space, the operators H, H^{-1} must be the pair of the Hilbert transform on the real axis (called the infinite Hilbert transform). It is well-known that the iteration of equation (9) converges to an element of $C = \cap_{i=1}^5 C_i$ if C is not empty, *i.e.* if there exist at least one solutions $f(t)$ compatible with the measured Hilbert transform $g(t)$ and all the other constraints (Youla and Webb 1982).

The most intensive computation in the POCS algorithm is the implementation of the operator P_1. In POCS-1, P_1 must be implemented using the infinite Hilbert transform to avoid data truncation in the Hilbert transform domain, because the support of $(Hf)(t)$ is $(-\infty, \infty)$ even if the support of $f(t)$ is a finite interval Λ. If the operator pair H, H^{-1} in POCS-1 can be replaced by the finite Hilbert transform pair (Tricomi 1957, Gakhov 1966, Pandy 1995), the computational cost will be significantly reduced thanks to the elimination of dealing with a function having infinite support. To achieve this aim, we propose an improved version of POCS-1 called POCS-2 below. First, we assume that $X = (-1, 1) \supseteq \Lambda$, where we recall that Λ denotes the interval corresponding to the object support. This assumption does not lose generality because, if $X \subset \Lambda$, we

can translate and rescale the t coordinate such that this condition is satisfied. Next, we define a weighted L^2 space $L^2_W(X)$ in which the inner product and the norm are defined by

$$(f_1, f_2)_W = \int_{-1}^{1} dt\ f_1(t) f_2(t) W(t),\ \| f \|^2_W = (f, f)_W$$
$$W(t) = \sqrt{1 - t^2}. \tag{12}$$

At this stage, the rationale behind using such a space may not be obvious. However, as explained later, this definition was intended to assure that the operator obtained by replacing H, H^{-1} in equation (10) by the finite Hilbert transform pair H_X, H_X^{-1} becomes the projection operator P_1. POCS-2 aims at finding $f(t) \in L^2_W(X)$ which belongs to the intersection of the following five convex sets:

$$C_1 = \{f \in L^2_W(X) \mid (H_X f)(t) = g(t) \text{ for } t \in \Lambda_H\}$$
$$C_2 = \{f \in L^2_W(X) \mid f(t) = 0 \text{ for } t \notin \Lambda\}$$
$$C_3 = \{f \in L^2_W(X) \mid f(t) = f^{(p)}(t) \text{ for } t \in \Lambda_K\}$$
$$C_4 = \{f \in L^2_W(X) \mid \int_{\Lambda \setminus \Lambda_K} dt\ f(t) = C^{(p)}_\Lambda\}$$
$$C_5 = \{f \in L^2_W(X) \mid f(t) \geq 0 \text{ for } t \in X\} \tag{13}$$

Now, X is a finite interval containing the object support Λ so that we need not deal with a function having infinite support in implementing the POCS algorithm. P_2, P_3, P_5 have again straightforward expressions (omitted here), and P_1, P_4 are expressed as

$$(P_1 f)(t) = (\frac{1}{\pi}\frac{1}{W(t)} \int_{-1}^{1} dt'\ f(t')) + (H^+_X M H_X f)(t)$$
$$(H_X f)(t) = \frac{1}{\pi}\ \text{p.v.} \int_{-1}^{1} ds\ \frac{1}{t-s} f(s)$$
$$(H^+_X h)(t) = \frac{1}{\pi}\frac{1}{W(t)} \text{p.v.} \int_{-1}^{1} ds\ \frac{1}{s-t} h(s) W(s)$$
$$(Mh)(t) = \begin{cases} g(t) & (t \in \Lambda_H) \\ h(t) & (t \notin \Lambda_H) \end{cases} \tag{14}$$

$$(P_4 f)(t) = \begin{cases} f(t) + \dfrac{(C^{(p)}_\Lambda - \displaystyle\int_{\Lambda \setminus \Lambda_K} dt'\ f(t'))/W(t)}{\displaystyle\int_{\Lambda \setminus \Lambda_K} dt'\ 1/W(t')}\ (t \in \Lambda \setminus \Lambda_K). \\ f(t) \quad (t \notin \Lambda \setminus \Lambda_K) \end{cases} \tag{15}$$

The derivation of P_4 is easy (omitted here). However, we need to prove that P_1 defined above is actually the projection operator onto the set C_1. This is not trivial because the finite Hilbert transform H_X is not a unitary transform unlike the infinite Hilbert transform. We leave the proof to Appendix C. The convergence proof of the POCS algorithm is valid for weighted norms as in equation (12) (Youla and Webb 1982), so that the convergence of POCS-2 to an element of $C = \cap_{i=1}^5 C_i$ is assured.

We confirmed that POCS-1 and POCS-2 achieve comparable image quality, but POCS-2 significantly reduces the computational cost by eliminating the necessity of involving a function having infinite support. In all the experimental results shown later, we used POCS-2. We also note that the choice of the interval X relative to Λ affects numerical behaviour (*i.e.* numerical stability and convergence speed) of POCS-2. We confirmed that a good choice of X when $\Lambda = (-0.6, 0.6)$ is $X = (-1, 1)$, *i.e.* the tight choice $X \simeq \Lambda$ was not good due to the singularities of $1/W(t) = (1-t^2)^{-1/2}$ at $t = \pm 1$.

3.3. Algorithm for Result 3

Reconstruction algorithms corresponding to Result 3 (non-convex ROI) become more complicated compared to that described in section 3.1. In this case, the proof of Result 3 suggests the following multi-step method. For a given configuration of the subsets (K, H, B), we first find a sequence of convex regions $A_1, A_2, \ldots, A_N$ ($N \geq 2$ is an arbitrary positive integer), such that (a) $B \cup (\cup_{i=1}^{N} A_i) = S$ (*i.e.* the union of $B, A_1, A_2, \ldots, A_N$ covers the whole ROI S), (b) $A_1 \cap B \neq \{\phi\}$ (*i.e.* A_1 contains a part of the region B), and (c) $D_i = (B \cup (\cup_{j=1}^{i-1} A_j)) \cap A_i \cap H \neq \{\phi\}$ for $i = 2, 3, \ldots, N$ (*i.e.* the union of the past regions $B \cup (\cup_{j=1}^{i-1} A_j)$ and the current region A_i have an intersection on the region H)‖. We show examples of valid sequences of convex regions $A_1, A_2, \ldots, A_N$ satisfying these conditions in figure 4(a),(b). Then, an exact algorithm can be constructed as follows. The main idea is to propagate information of the object $f(x, y)$ on the region B along the polygonal or tree-structured link of the convex regions $A_1, A_2, \ldots, A_N$ (as in the proof of Result 3). First, the reconstruction is performed on the region A_1 which allows us to use information of $f(x, y)$ on the set D_2 in the next step. Next, the reconstruction is performed on the region A_2 by taking the set D_2 as the region B, the reconstruction is performed on the region A_3 by taking the set D_3 as the region B, and this process is repeated till A_N to complete the reconstruction on the whole ROI S.

In figure 4(a), we show a typical example of the multi-step method. In this example, the reconstruction is performed according to the following three steps. The lines with an arrow in the figure represent a set of the Hilbert lines along which the DBP and the Hilbert inversion are performed at each step. The first step reconstructs $f(x, y)$ on the left rectangular region A_1. By using $f(x, y)$ on the set D_2 obtained in the first step, the second step reconstructs $f(x, y)$ on the bottom rectangular region A_2 reaching to the part D_3 of the right rectangular region A_3. The third step reconstructs $f(x, y)$ on the right region A_3 by using $f(x, y)$ on the set D_3 obtained in the second step. It is likely that the similar multi-step methods can be empirically designed for many other imaging configurations. It is still an open problem to clarify a general mechanism to design such an efficient method for every case satisfying the conditions of Result 3.

‖ The two convex regions (A_i, A_j) $(i \neq j)$ can overlap.

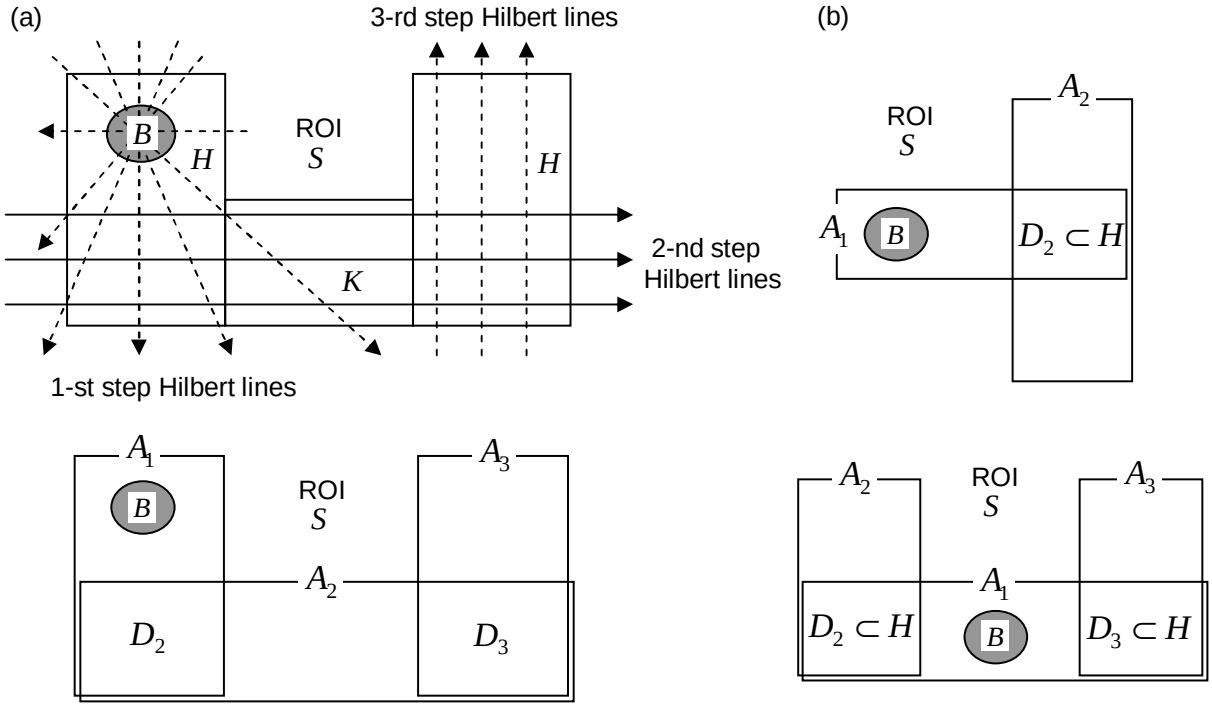

Figure 4. (a) An example of the multi-step reconstruction method corresponding to Result 3. In the first step, the reconstruction is performed on the set of the 1-st step Hilbert lines (polar broken lines). In the second step, the reconstruction is performed on the set of the 2-nd step Hilbert lines (real lines). In the third step, the reconstruction is performed on the set of the 3-rd step Hilbert lines (parallel broken lines). The corresponding choice of the polygonal link of the convex regions A_1, A_2, A_3 is also shown. (b) Other examples of the valid sequence of convex regions $A_1, A_2, \ldots, A_N$.

4. Experimental Results

4.1. Simulation Studies

We first performed three simulation studies each of which corresponds to Result 1, Result 2, or Result 3. Throughout the simulations, we used the Shepp-Logan phantom. The ordinary definition of the Shepp-Logan phantom was enlarged 2.5 times such that it is contained inside a square of side 5.0, where we placed a square ROI of side 2.0 at the center (figure 5). We computed 1,200 parallel-beam projections over 180° angular range with the radial sampling $\Delta r = 2.0/256$, and then truncated them such that rays not passing through the region H are not used for reconstruction dependent on each situation (recall that H always contains B). Reconstructed images consist of 256×256 pixels with the sampling $\Delta x = \Delta y = 2.0/256$ for every case. The iteration number of POCS-2 in the Hilbert inversion was 500, and the object support constraint C_2 was enforced by assuming that the object is known *a priori* to be contained inside an ellipse which is 1.2 times larger than the true object boundary (figure 5).

In figure 6 (left), we show the setup of Simulation 1 corresponding to Result 1, where the Hilbert transform $g_\theta(x, y)$ is known on the whole ROI and we know the

object $f(x, y)$ *a priori* on the thin strip B of size 0.1×2.0 located at the center. The natural choice of the Hilbert lines in this setup is horizontal as shown in figure 3(a). We show a reconstructed image (left) together with a reconstructed image when the *a priori* knowledge on $f(x, y)$ is not available (right) (figure 6). As is observed, without the *a priori* knowledge on $f(x, y)$, the reconstructed image suffered from the DC shifts and the low-frequency artifacts. In figure 7 (top left), we show the setup of Simulation 2 corresponding to Result 2, where the Hilbert transform $g_\theta(x, y)$ is known on the right region H, the object $f(x, y)$ is known on the left region K, and both $g_\theta(x, y)$ and $f(x, y)$ are known on the thin strip B of size 0.1×2.0 located at the left edge. The natural choice of the Hilbert lines in this setup is again horizontal. To demonstrate that the conditions of Result 2 are important for accurate reconstruction, we tried reconstructions for three other configurations of (K, H, B) which do not satisfy the conditions of Result 2. We show reconstructed images for all the cases (figure 7). As is observed, for all the cases where the configuration of (K, H, B) does not satisfy the conditions of Result 2, the reconstructed images suffered from the DC shifts and the low-frequency artifacts. In figure 8 (left), we show the setup of Simulation 3 corresponding to Result 3, where the ROI is a (reversed) L-shaped region, the Hilbert transform $g_\theta(x, y)$ is known on the right region, we know the object $f(x, y)$ *a priori* on the left bottom rectangle, and both $g_\theta(x, y)$ and $f(x, y)$ are known on the strip B of size 0.2×0.5 located at the left edge. The reconstruction was performed according to the following two-step method (section 3.3). The first step reconstructs $f(x, y)$ on the bottom rectangular region by taking the Hilbert lines as a set of horizontal lines (broken lines). The second step reconstructs $f(x, y)$ on the right rectangle by taking the Hilbert lines as a set of vertical lines (real lines). We show a reconstructed image (figure 8).

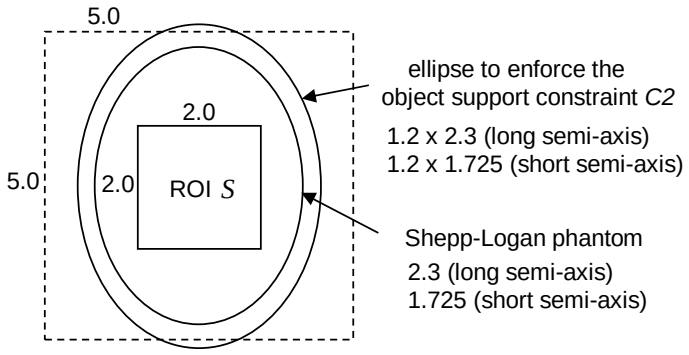

Figure 5. The phantom and the ROI S in the simulation studies.

We also performed the above three simulations with noisy projection data. The Poisson noise corresponding to 1.0×10^6 incident photons per detector bin was added to the projection data, by assuming the length of the long semi-axis of the phantom to be 20 (cm) and the realistic values of attenuation coefficients in x-ray CT. In figure 6 (bottom), we show reconstructed images corresponding to the setup of Simulation 1. Furthermore, for each setup (Simulation 1, Simulation 2, Simulation 3), we evaluated

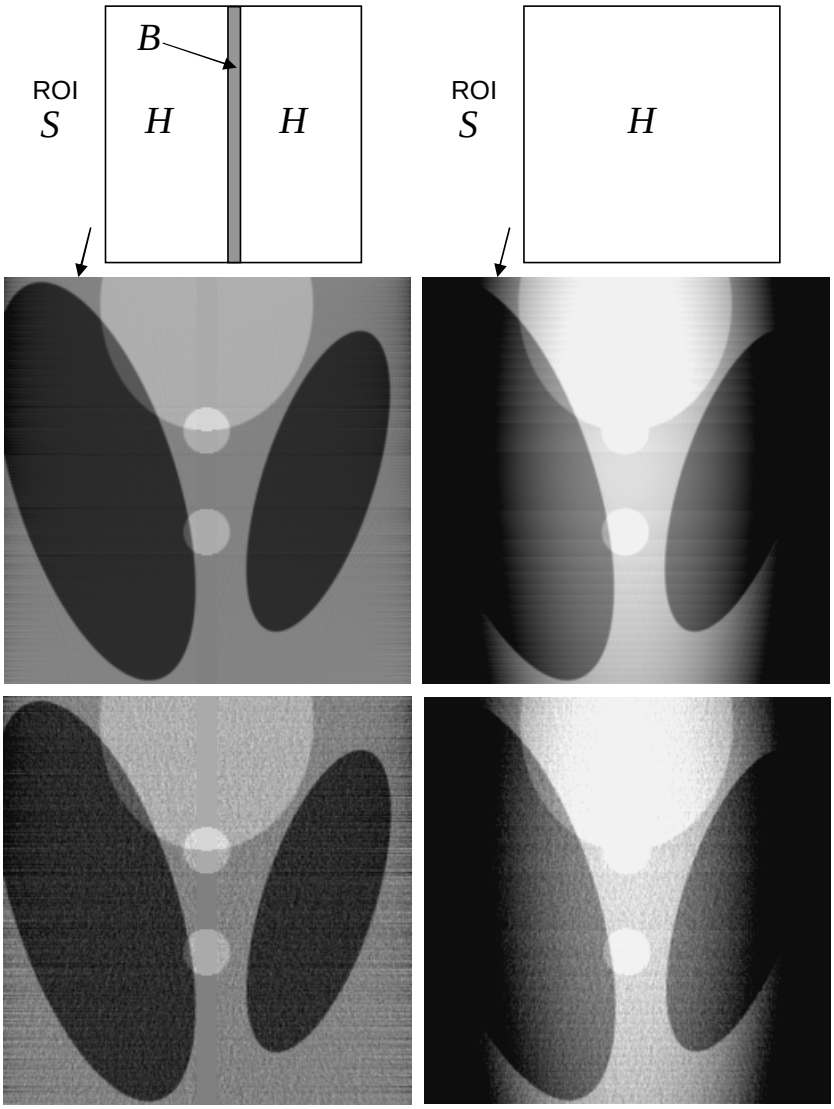

Figure 6. Reconstructed images in the Simulation 1. The left images were reconstructed by using the *a priori* knowledge of $f(x, y)$ on the thin strip region B. The right images were reconstructed without the *a priori* knowledge. The display window was set to [0.994,1.046] for the left images, and was set to [0.874,0.926] for the right images to make the low-frequency artifacts other than the DC shifts visible. The top images are reconstructions without noise and the bottom images are reconstructions with noise.

the root mean square value of noise $RMSN$ in the ROI $S \setminus K$:

$$RMSN = \sqrt{\frac{\sum_{(i,j)\in S\setminus K} (f_n(i,j) - f(i,j))^2}{\sum_{(i,j)\in S\setminus K} 1}}, \tag{16}$$

where $f_n(i, j)$ denotes the reconstructed image with noise and $f(i, j)$ denotes the reconstructed image without noise. The value of $RMSN$ was computed for both the

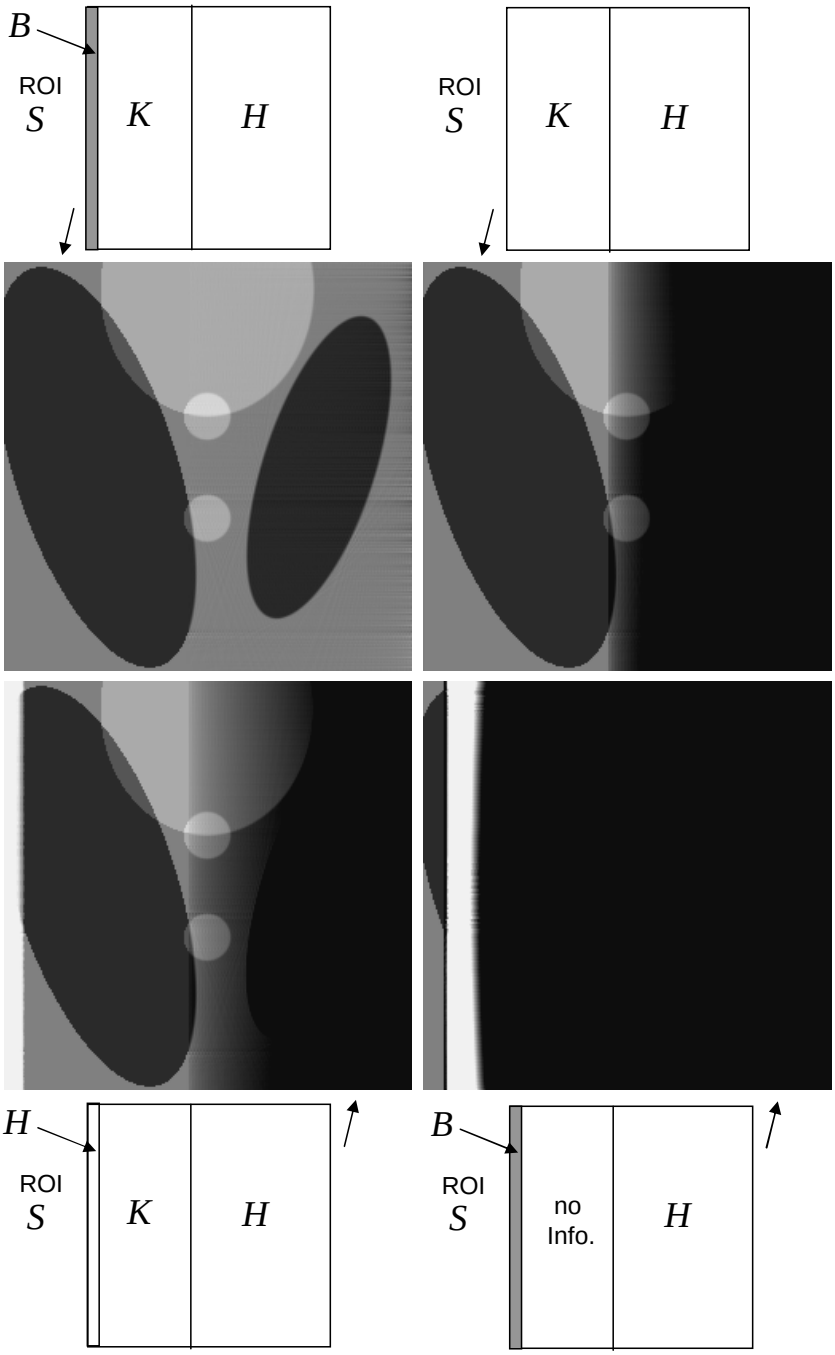

Figure 7. Reconstructed images in the Simulation 2. The top left image was reconstructed from the configuration of (K, H, B) satisfying the conditions of Result 2. The other three images were reconstructed from the configurations violating the conditions of Result 2. The display window was set to [0.994,1.046] for all the images.

DBP-POCS method (with truncated projection data) and the standard FBP method (with non-truncated projection data). To make this comparison fair, we applied the post-smoothing filter to the FBP image such that the spatial resolution of FBP image approximately matches to that of DBP-POCS image. We summarize the result in

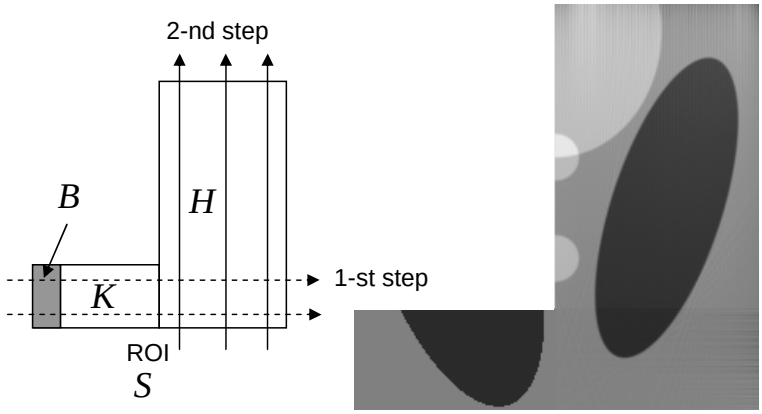

Figure 8. Reconstructed image in the Simulation 3 where the configuration of (K, H, B) satisfies the conditions of Result 3. The display window was set to [0.994,1.046].

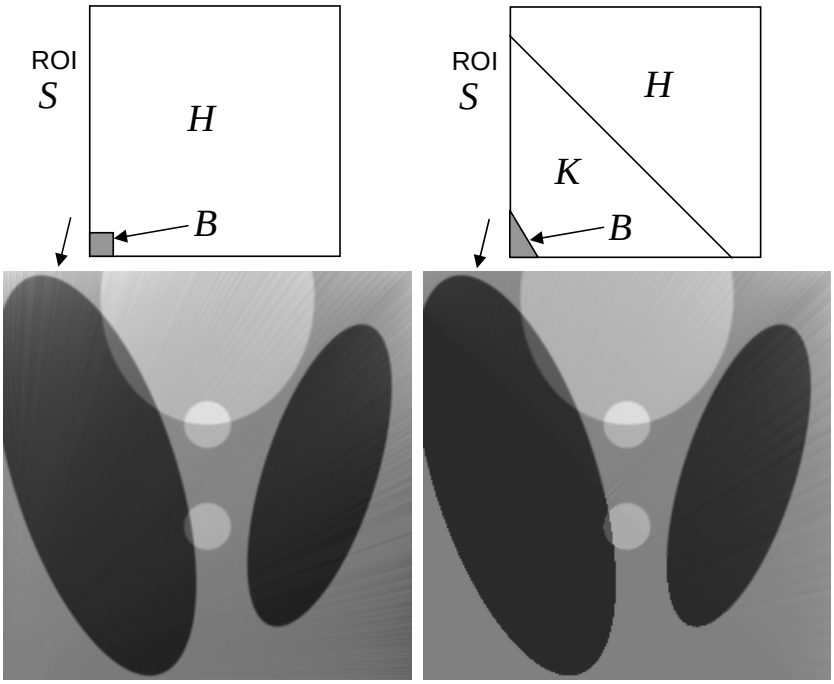

Figure 9. Reconstructed images in the Simulation 4. The setup in the left case corresponds to Result 1 and the setup in the right case corresponds to Result 2. The display window was set to [0.994,1.046] for the both images. Though not shown here, the reconstructed images suffered from the DC shifts and the low-frequency artifacts when we changed the setups such that only one of the Hilbert transform $g_\theta(x, y)$ and the object $f(x, y)$ is available on the region B.

table 1. This result demonstrates that the noise propagation of DBP-POCS method is comparable to that of FBP method, and the inversion with truncated data is much more stable compared to other limited-data problems such as the limited-angle and exterior problems (Natterer 1986) as long as the conditions for uniqueness shown in this paper are satisfied.

Table 1. Root mean square value of noise $RMSN$ in the ROI $S \setminus K$.

Reconstruction method	Simulation 1	Simulation 2	Simulation 3
DBP-POCS (truncation)	1.27×10^{-2}	1.24×10^{-2}	1.56×10^{-2}
FBP (no truncation)	1.17×10^{-2}	1.18×10^{-2}	1.15×10^{-2}

4.2. Polar Hilbert Lines

In all the simulation studies in section 4.1, the region B was a thin strip as shown in figure 3(a) so that a set of Hilbert lines $L(u);\ u \in U$ could be chosen as the horizontal or vertical lines. In this case, the coordinate transform (Step 4 of the algorithm summary in section 3.1) to convert reconstructed images represented on the (u, t) coordinates to those on the (x, y) coordinates can be avoided. However, such a simplification does not occur when the region B is a small square or circular region as shown in figure 3(b). In this case, a set of Hilbert lines must be chosen as a set of polar lines having its origin at a point in the region B so that reconstructed images must be interpolated from the (u, t) coordinates to the (x, y) coordinates after the Hilbert inversion. We performed a simulation study (Simulation 4) in this case. We show the setups of Simulation 4 together with reconstructed images (figure 9), where the left example corresponds to Result 1 and the right example corresponds to Result 2. The other conditions in the simulation were same as those in section 4.1. As is observed, the overall tendency of the results was similar to those explained in section 4.1.

4.3. Real CT Data

We performed reconstructions of real (head) CT data acquired with a third generation CT scanner. The sampling of the acquired fan-beam projection data was 512(channels)×600(views). This data was rebinned into the parallel-beam data consisting of 512(bins)×1,000(angles), which was used for reconstructions. As shown in figure 10 (top) (superimposed on the FBP reconstruction using the complete projection data), we placed a rectangular ROI consisting of 160×120 pixels at the center of the object. We considered two setups of the configuration of the subsets (K, H, B) as shown in figure 10 (left). The first setup corresponds to Result 1 and the second setup corresponds to Result 2. The natural choice of the Hilbert lines was horizontal for the both setups. The object support constraint C_2 was enforced by assuming that the object $f(x, y)$ is known *a priori* to be contained inside an ellipse which is approximately 1.2 times larger than the true object boundary. For the use of *a priori* knowledge on $f(x, y)$, we considered the following three scenarios.

[Scenario 1] (Perfect *a priori* knowledge) On the region K (recall that K always contains B), the *a priori* knowledge of $f(x, y)$ is created from the FBP reconstruction using the complete data. ∎

[Scenario 2] (Imperfect *a priori* knowledge) On the region K (K always contains B), we regard $f(x, y)$ as a constant function, *i.e.* $f(x, y) = \alpha$ =const. for $(x, y) \in K$. The value of the constant α is created by computing an average of the FBP reconstruction using the complete data over K. ∎

[Scenario 3] (No *a priori* knowledge) On the region K (K always contains B), the *a priori* knowledge of $f(x, y)$ is not available at all. ∎

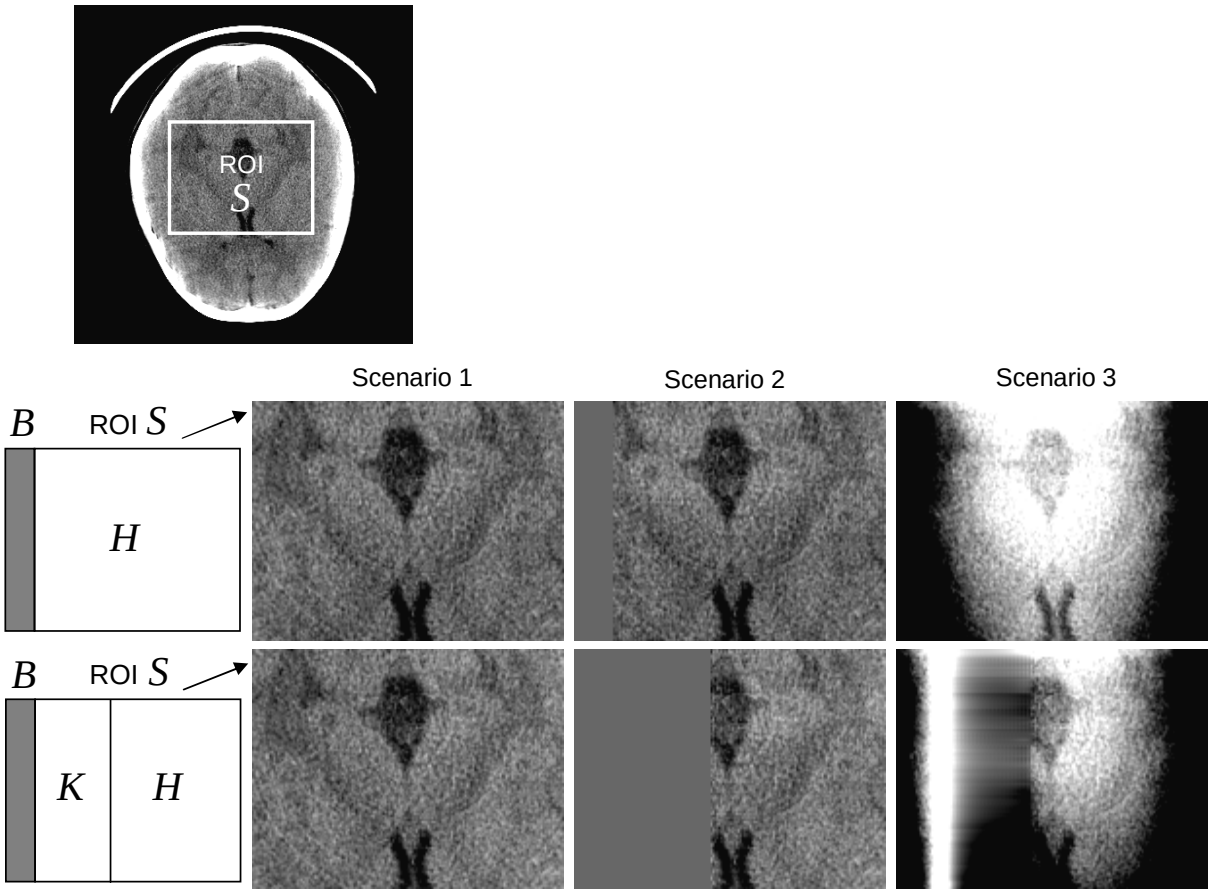

Figure 10. Reconstructed images from real CT data. The top figure shows the location of the ROI S superimposed on the FBP reconstruction using the complete projection data. The middle row shows reconstructed images corresponding to the setup of Result 1. The bottom row shows reconstructed images corresponding to the setup of Result 2. For each setup, we compared the three scenarios on how to create the *a priori* knowledge on the object, *i.e.* Scenario 1 (perfect *a priori* knowledge), Scenario 2 (imperfect *a priori* knowledge), and Scenario 3 (no *a priori* knowledge). The display window was set to [0HU,80HU] for the cases of Scenario 1 and Scenario 2, and was set to [-320HU,-240HU] for the case of Scenario 3 to make the low-frequency artifacts other than the DC shifts visible.

We show reconstructed images in figure 10. The images without the *a priori* knowledge (Scenario 3) suffered from the DC shifts and the severe low-frequency artifacts as expected. On the other hand, the cases of Scenario 1 and Scenario 2 succeeded in producing acceptable images. In particular, the case of Scenario 2 produced the

surprisingly good reconstructions comparable to those of Scenario 1. This result let us think that the inversion is not sensitive to accuracy of the *a priori* knowledge on the object. It is likely that even a rough knowledge on the object such as an estimate of the average value of the object on some region K is sufficient to dramatically improve image quality.

4.4. POCS-1 vs. POCS-2

For the Hilbert inversion, the main advantage of newly developed POCS-2 over POCS-1 is that POCS-2 does not involve the Hilbert transform function having infinite support $(Hf)(t)$ $(-\infty < t < \infty)$. To demonstrate that this advantage leads to a significant reduction in computational cost, we investigated how reconstructed images are degraded when POCS-1 is approximately implemented by truncating the interval to compute the function $(Hf)(t)$ to a finite interval $t \in X$. In the setup of Simulation 1 where the object support and the ROI on each Hilbert line $L(u)$ are $\Lambda \approx (-2.0, 2.0)$ (512 sampling points) and $\Lambda_S = (-1.0, 1.0)$ (256 sampling points), we performed the Hilbert inversion by the approximate POCS-1 implementation with three different intervals X, which are $X = (-4.0, 4.0)$ (1,024 sampling points), $X = (-16.0, 16.0)$ (4,096 sampling points), and $X = (-32.0, 32.0)$ (8,192 sampling points). For a comparison, we also implemented POCS-2 in which the same intervals X as above were used as the whole interval to define the finite Hilbert transform function $(H_X f)(t)$ $(t \in X)$. We show reconstructed images (figure 11). As expected, when the interval X was not sufficiently large, the images by the approximate POCS-1 implementation suffered from the severe DC shifts and the low-frequency artifacts due to the data truncation of the Hilbert transform function $(Hf)(t)$ outside X. On the other hand, the images by POCS-2 did not depend on the choice of the interval X (unless X is too close to the object support Λ). In this setup, to make the truncation error of the function $(Hf)(t)$ almost negligible, POCS-1 had to be implemented with $X = (-32.0, 32.0)$, whereas $X = (-4.0, 4.0)$ was enough in POCS-2. The computational time of POCS-1 with $X = (-32.0, 32.0)$ was approximately eighteen times longer than that of POCS-2 with $X = (-4.0, 4.0)$ (FFT was used to compute the Hilbert transform). The superiority of POCS-2 to POCS-1 is apparent from this experiment.

4.5. High-Contrast Objects

The Shepp-Logan phantom and the real data used in section 4.3 primarily consist of low-contrast structures. An evaluation with a more challenging phantom containing high-contrast structures would be interesting. Therefore, we performed an additional simulation study (Simulation 5) using the FORBILD thorax phantom which contains the high-contrast structures corresponding to the lung and the vertebra (an object simulating the heart was added as in Defrise *et al* 2006). A rectangular ROI was placed at the center. The conditions and the setups of the simulation were made similar to those in section 4.1. We show the setups of Simulation 5 together with reconstructed

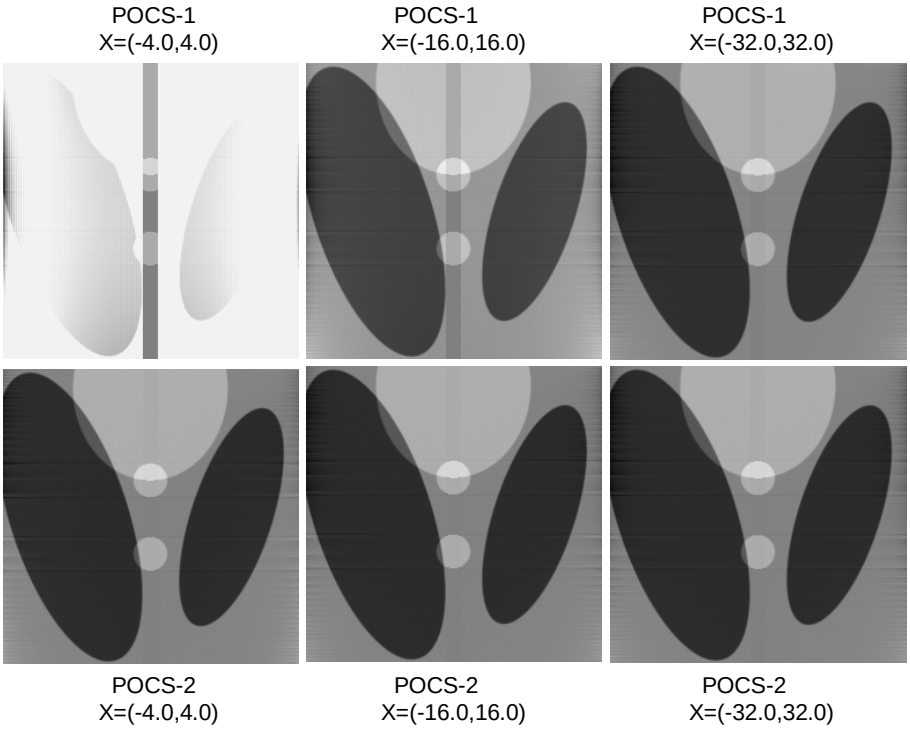

Figure 11. (Top) Reconstructed images by the approximate POCS-1 Hilbert inversion in which the interval X to compute the Hilbert transform function $(Hf)(t)$ was truncated to $X = (-4.0, 4.0)$, $X = (-16.0, 16.0)$, and $X = (-32.0, 32.0)$. The object support was $\Lambda \approx (-2.0, 2.0)$ in this setup. (Bottom) Reconstructed images by the POCS-2 Hilbert inversion in which the same intervals X as above were used as the whole interval to define the finite Hilbert transform function $(H_X f)(t)$ (of course, in the implementation, the t coordinate was rescaled such that $X = (-1, 1)$ to use the equations in section 3.2). The display window was set to [0.994,1.046] for all the images.

images (figure 12), where the left example corresponds to Result 1 and the right example corresponds to Result 2. The streak artifacts were a bit stronger along tangential directions of the high-contrast objects compared to the case of Shepp-Logan phantom, but the DC shifts and the severe low-frequency artifacts were not observed.

5. Conclusions and Discussions

In this paper, based on the concept of DBP combined with the Hilbert inversion (Noo *et al* 2004, Pan *et al* 2005, Defrise *et al* 2006), we showed that the solution to the interior problem in CT is unique if a tiny *a priori* knowledge on the object $f(x, y)$ is available in the form that $f(x, y)$ is known on a small region located inside the ROI (Result 1). Furthermore, we advanced the uniqueness result to obtain more general uniqueness results which can be applied to a wider class of imaging configurations (Result 2, Result 3, Result 4, Result 5). We also developed a reconstruction algorithm which can be considered an extension of the DBP-POCS method described by Defrise *et al* (2006), where we proposed a new POCS algorithm (POCS-2) for the Hilbert inversion which

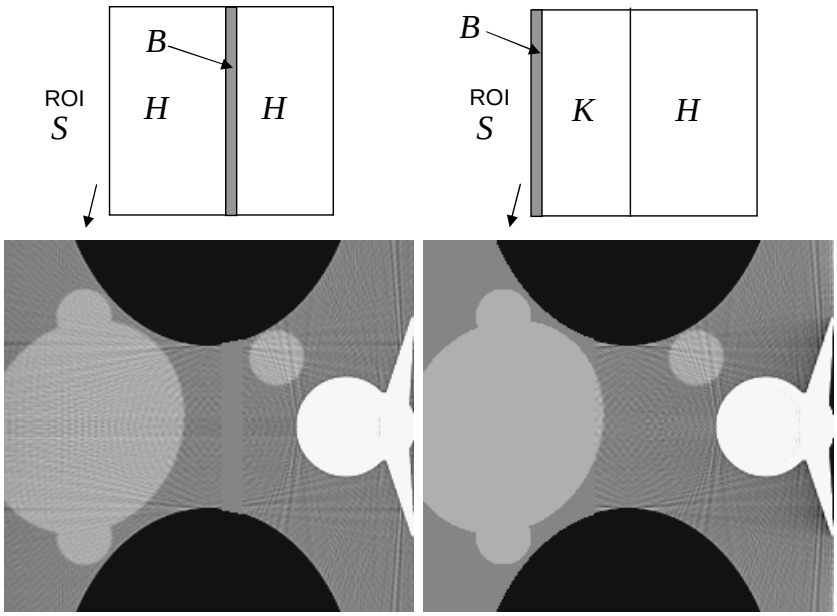

Figure 12. Reconstructed images of the FORBILD thorax phantom (Simulation 5). The setup in the left case corresponds to Result 1 and the setup in the right case corresponds to Result 2. The display window was set to [0.922,1.078] for the both images.

significantly reduces computational cost of the DBP-POCS method.

Finally, we would like to make the following discussions. First, we note that a stronger uniqueness result has been already obtained in our companion work (Courdurier 2007a, 2007b) using the Plemelj-Sokhotskii formula in complex analysis (Gakhov 1966), which says that, if the region B (on which both the Hilbert transform and the object are known) is non-empty, the object having a finite support is uniquely determined on the whole 2-D space. The uniqueness results proved in this paper (using a different mathematical technique) are weaker than that in Courdurier 2007a, 2007b. However, the uniqueness does not imply the stability, *i.e.* the inversion can be severely unstable, in the sense that the solution does not depend continuously on the data even if it is unique, as in the limited-angle problem (Natterer 1986). Therefore, the most valuable contribution of this paper was to show evidence of the stability for Result 1, Result 2, and Result 3 by the experimental results. Second, we note that, again in our companion work (Courdurier 2007a, 2007b), the stability has been theoretically analyzed for Result 1 using Nevanlinna's principle (Defrise *et al* 2006). We think that the similar stability analysis is possible for Result 2 and Result 3 because the main mathematical tool to prove the uniqueness for these cases was a combination of the analytic continuations (similar to that in Defrise *et al* 2006). We leave it as a future work. Another practical issue would be to develop methods to acquire the *a priori* knowledge on the object in various imaging situations.

As described in the introduction, there is some overlap between our work and that published by Ye *et al* (2007). The overlap lies in Result 1, which was discovered,

independently and at the same time, by Ye *et al* (2007). To the best of our knowledge, the uniqueness results and reconstruction algorithms corresponding to Result 2, Result 3, Result 4, Result 5 and POCS-2 are original contributions.

Appendix A. Analyzing Integral Equation of Equation (5)

We assume that $a \geq -1$ and $f \leq 1$ for simplicity. This assumption does not lose generality because we can translate and rescale the t coordinate (such that $-1 \leq a < f \leq 1$) if $a < -1$ or $f > 1$. Then, the inversion formula of the finite Hilbert transform (Tricomi 1957, Gakhov 1966, Pandy 1995) is written as

$$\begin{aligned}
&\sqrt{1-t^2}f(t) = h_1(t) + h_2(t) \\
&h_1(t) = C_{af} + \frac{1}{\pi}\ \text{p.v.} \int_b^e ds\ \frac{1}{s-t} g(s)\sqrt{1-s^2} \\
&h_2(t) = \frac{1}{\pi}\ \text{p.v.}(\int_{-1}^b + \int_e^1) ds\ \frac{1}{s-t} g(s)\sqrt{1-s^2}.
\end{aligned} \tag{A.1}$$

We can compute $h_1(t)$ from the measured Hilbert transform $g(t)$ for $t \in (b, e)$ and the known constant C_{af}. However, $h_2(t)$ cannot be computed because we do not have $g(t)$ for $t \in (-1, b) \cup (e, 1)$. Therefore, we use the analytical continuation described by Defrise *et al* (2006) as follows. Since we know $f(t) = f^{(p)}(t)$ for $t \in (c, d)$, we have $h_2(t)$ for $t \in (c, d)$ from

$$h_2(t) = \sqrt{1-t^2} f^{(p)}(t) - h_1(t) \text{ for } t \in (c, d). \tag{A.2}$$

If we replace t in $h_2(t)$ by the complex variable $z \in \mathbb{C}$, $h_2(z)$ is an analytic function in the complex plane having cuts along the segments $z \in (-1, b) \cup (e, 1)$ on the real axis. The analyticity follows from the fact that $h_2(z)$ having the form of equation (A.1) is an analytic function if $g(t)$ is a continuous function, which is the case because we assumed $f(t)$ to be continuous (see pp.39 in Dennery and Krzywicki 1967). Therefore, $h_2(z)$ can be analytically continued from the known interval (c, d) on the real axis to the larger interval (b, e) on the real axis. Since both $h_1(t)$ and $h_2(t)$ are uniquely determined for $t \in (b, e)$, $f(t)$ is uniquely determined for $t \in (b, e)$.

Appendix B. Analyzing Integral Equation of Equation (6)

First, we prepare two lemmas used to analyze equation (6). Let $f(t)$ be a continuous function having a support on $X = (-1, 1)$. Let $g(t)$ denote the Hilbert transform of $f(t)$. We take three points on the t coordinate (a, b, c) such that $-1 < a < b < c < 1$. Then, the following two lemmas can be proved.

[Lemma 1] Assume that (a) both $f(t)$ and $g(t)$ are known for $t \in (a, b)$ and (b) $g(t)$ is known for $t \in (b, c)$. Then, both $f(t)$ and $g(t)$ are uniquely determined for $t \in (a, c)$.

Proof: Omitted because this is just a special case of Appendix A. ∎

[Lemma 2] Assume that (a) both $f(t)$ and $g(t)$ are known for $t \in (a, b)$ and (b) $f(t)$ is known for $t \in (b, c)$. Then, both $f(t)$ and $g(t)$ are uniquely determined for $t \in (a, c)$.

Proof: The Hilbert transform $g(t)$ is written as

$$\begin{aligned} g(t) &= h_1(t) + h_2(t) \\ h_1(t) &= \frac{1}{\pi}\ \text{p.v.} \int_a^c ds\ \frac{1}{t-s} f(s) \\ h_2(t) &= \frac{1}{\pi}\ \text{p.v.} \left(\int_{-1}^a + \int_c^1 \right) ds\ \frac{1}{t-s} f(s). \end{aligned} \tag{B.1}$$

Now, $h_1(t)$ is a known function because we know $f(t)$ for $t \in (a, c)$. However, $h_2(t)$ is an unknown function because we do not know $f(t)$ for $t \in (-1, a) \cup (c, 1)$. Therefore, we use again the analytical continuation described by Defrise *et al* (2006) as follows. Since we know $g(t)$ for $t \in (a, b)$, we have $h_2(t)$ for $t \in (a, b)$ from

$$h_2(t) = g(t) - h_1(t) \text{ for } t \in (a, b). \tag{B.2}$$

If we replace t in $h_2(t)$ by the complex variable $z \in \mathbb{C}$, $h_2(z)$ is an analytic function in the complex plane having cuts along the segments $z \in (-1, a) \cup (c, 1)$ on the real axis. Therefore, $h_2(z)$ can be analytically continued from the known interval (a, b) on the real axis to the larger interval (a, c) on the real axis. The analyticity again follows from the continuity of $f(t)$ as in Appendix A. Since both $h_1(t)$ and $h_2(t)$ are uniquely determined for $t \in (a, c)$, $g(t)$ is uniquely determined for $t \in (a, c)$ so that both $f(t)$ and $g(t)$ are unique for $t \in (a, c)$. ∎

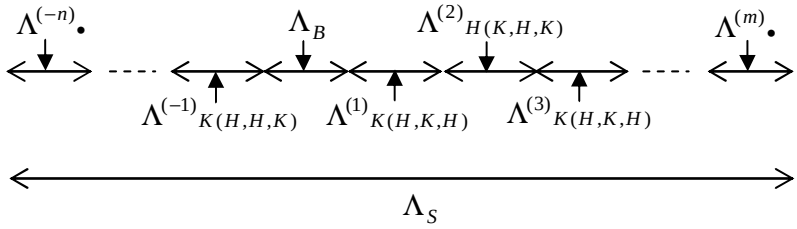

Figure B1. The configuration of the intervals $(\Lambda_S, \Lambda_K, \Lambda_H, \Lambda_B)$ necessarily takes the form shown in this figure.

We are ready to analyze the uniqueness for equation (6). We assume that $X = (-1, 1) \supseteq \Lambda$ for simplicity. This assumption does not lose generality because we can translate and rescale the t coordinate such that this condition is satisfied. Note that $X \supseteq \Lambda \supset \Lambda_S$. From equation (7), it is easy to know that the configuration of the intervals $(\Lambda_S, \Lambda_K, \Lambda_H, \Lambda_B)$ necessarily takes the form shown in figure B1, *i.e.* Λ_H and Λ_K alternate in the both sides of Λ_B¶. First, both $f(t)$ and $g(t)$ are known on Λ_B (located at the center). Therefore, by using Lemma 1 or Lemma 2, we can show that both $f(t)$ and $g(t)$ are unique for $t \in \Lambda_B \cup \Lambda^{(1)}_{K(H,K,H)}$. By using Lemma 1 or Lemma 2 again, we can show that both $f(t)$ and $g(t)$ are unique for $t \in \Lambda_B \cup \Lambda^{(1)}_{K(H,K,H)} \cup \Lambda^{(2)}_{H(K,H,K)}$. By repeating this process, the interval on which both $f(t)$ and $g(t)$ are unique can be enlarged unless the two successive subsets $\Lambda^{(i)}_{\cdot}, \Lambda^{(i+1)}_{\cdot}$ are disjoint, which never occurs.

¶ Figure B1 assumes that Λ_B is a single interval for simplicity. The proof for the case where Λ_B is a union of disjoint intervals is very similar.

We repeat this process till $\Lambda_\cdot^{(m)}$ in the positive direction. We do the same in the negative direction starting from Λ_B till $\Lambda_\cdot^{(-n)}$. Since Λ_S is the union of Λ_B and all $\Lambda_\cdot^{(i)}$ $(i = -n, \ldots, -1, 1, \ldots, m)$, both $f(t)$ and $g(t)$ are uniquely determined on Λ_S.

Appendix C. Projection Operator P_1

The proof of the projection operator P_1 is based on the norm equivalence (weighted orthogonality) of the finite Hilbert transform (with $W(t)$ defined by equation (12)):

$$\int_{-1}^{1} dt\ f^2(t)W(t) = \int_{-1}^{1} dt\ (H_X f)^2(t)W(t) + \pi C_X^2$$
$$C_X = \frac{1}{\pi}\int_{-1}^{1} dt\ f(t) \tag{C.1}$$

For unfamiliar readers, using the operators H_X, H_X^+ defined by equation (14), the inversion formula of the finite Hilbert transform (Tricomi 1957, Gakhov 1966, Pandy 1995), and the property $(f, H_X^+ h)_W = (H_X f, h)_W$ which holds for any functions $f(t) \in L_W^2(X), h(t) \in L_W^2(X)$, we give a derivation of equation (C.1) as follows.

$$\begin{aligned}
\text{L.H.S.} &= (f(t), f(t))_W \\
&= (f(t), \frac{C_X}{W(t)} + (H_X^+ H_X f)(t))_W \\
&= (f(t), \frac{C_X}{W(t)})_W + ((H_X f)(t), (H_X f)(t))_W \\
&= C_X \int_{-1}^{1} dt\ f(t) + \parallel (H_X f)(t) \parallel_W^2 \\
&= \pi C_X^2 + \parallel (H_X f)(t) \parallel_W^2 = \text{ R.H.S.}
\end{aligned} \tag{C.2}$$

From the definition of the projection operator, given $f(t)$, we would like to find $\tilde{f}(t) \equiv (P_1 f)(t) \in C_1$ minimizing $\parallel f - \tilde{f} \parallel_W^2$. From equation (C.1), the minimized function reduces to

$$\parallel f - \tilde{f} \parallel_W^2 = \parallel H_X f - H_X \tilde{f} \parallel_W^2 + \pi D_X^2$$
$$D_X = \frac{1}{\pi}\int_{-1}^{1} dt\ (f(t) - \tilde{f}(t)). \tag{C.3}$$

From the inversion formula of the finite Hilbert transform (Tricomi 1957, Gakhov 1966, Pandy 1995), the general solution minimizing the first term $\parallel H_X f - H_X \tilde{f} \parallel_W^2$ subject to $\tilde{f}(t) \in C_1$ can be written as

$$\tilde{f}(t) = \frac{1}{W(t)}(C + \frac{1}{\pi}\ \text{p.v.} \int_{-1}^{1} ds\ \frac{1}{s-t}\tilde{h}(s)W(s))$$
$$\tilde{h}(t) = \begin{cases} g(t) & (t \in \Lambda_H) \\ (H_X f)(t) & (t \notin \Lambda_H), \end{cases} \tag{C.4}$$

where C is an arbitrary constant which arises due to the null space of the finite Hilbert transform, *i.e.* the finite Hilbert transform of $1/W(t) = (1-t^2)^{-1/2}$ vanishes on the

whole X (Tricomi 1957, Gakhov 1966, Pandy 1995). Note that the function $\tilde{f}(t)$ in the form of equation (C.4) minimizes $\| H_X f - H_X \tilde{f} \|_W^2$ for any value of C. Therefore, the problem of finding $\tilde{f}(t)$ reduces to determining the constant C minimizing the second term πD_X^2 in equation (C.3). Substituting equation (C.4) into $D_X = 0$ and using the property (which holds for any $\tilde{h}(s)$)

$$\int_{-1}^{1} dt \ (\frac{1}{W(t)} \text{p.v.} \int_{-1}^{1} ds \ \frac{1}{s-t} \tilde{h}(s) W(s)) = 0, \tag{C.5}$$

we have

$$\int_{-1}^{1} dt \ (f(t) - \frac{C}{W(t)}) = 0. \tag{C.6}$$

Solving equation (C.6) for C yields

$$C = \frac{1}{\pi} \int_{-1}^{1} dt \ f(t). \tag{C.7}$$

Equation (C.4) with C given by equation (C.7) is same as the expression of P_1 in equation (14). This completes the proof.

References

Clackdoyle R, Noo F, Guo G and Roberts J A 2004 Quantitative reconstruction from truncated projections in classical tomography *IEEE Trans.Nucl.Sci.* **51** 2570-2578

Combettes P 1993 The foundations on set-theoretic estimation *Proc.IEEE* **81** 182-208

Courdurier M 2007a La transformada de Rayos X: El problema interior con conocimiento *a priori* *Seminar at Centro De Modelamiento Matematico* (Centro de Modelamiento Matematico, Chile) http://www.cmm.uchile.cl/doc/seminarios/anuncio_16_30_3_1_2007_2.pdf

Courdurier M 2007b Solving the interior problem in computed tomography using *a priori* knowledge *Conference on Applied Inverse Problems 2007: Theoretical and Computational Aspects* (Vancouver, Canada)

Defrise M, Noo F, Clackdoyle R and Kudo H 2006 Truncated Hilbert transform and image reconstruction from limited tomographic data *Inverse Problems* **22** 1037-1053

Dennery P and Krzywicki A 1967 *Mathematics for Physicists* (New York: Dover)

Gakhov F D 1966 *Boundary Value Problems* (New York: Dover)

Gelfand I M and Graev M I 1991 Crofton's function and inversion formula in real integral geometry *Functional Analysis and Its Applications* **25** 1-5

Kudo H 2006 Analytical image reconstruction methods for medical tomography -Recent advances and a new uniqueness result *Proceedings of Mathematical Aspects of Image Processing and Computer Vision 2006* (Sapporo, Japan) Paper No. 00001652 http://eprints.math.sci.hokudai.ac.jp/archive/00001652/

Kudo H, Courdurier M, Noo F and Defrise M 2007 Tiny *a priori* knowledge solves the interior problem *Conference Record of 2007 IEEE Nuclear Science Symposium and Medical Imaging Conference* (Honolulu, U.S.A.) Paper No. M21-1

Lewitt R M 1979 Processing of incomplete measurement data in computed tomography *Med.Phys.* **6** 412-417

Louis A K and Rieder A 1989 Incomplete data problems in x-ray computerized tomography II. Truncated projections and region-of-interest tomography *Num.Math.* **56** 371-383

Maass P 1992 The interior Radon transform *SIAM J.Appl.Math.* **52** 710-724

Natterer F 1986 *The Mathematics of Computerized Tomography* (New York: Wiley)

Noo F, Clackdoyle R and Pack J D 2004 A two-step Hilbert transform method for 2D image reconstruction *Phys.Med.Biol.* **49** 3903-3923

Ogawa K, Nakajima M and Yuta S 1984 A reconstruction algorithm from truncated projections *IEEE Trans.Med.Imaging* **3** 34-40

Ohnesorge B, Flohr T, Schwarz K, Heiken J P and Bae K T 2000 Efficient correction for CT image artifacts caused by objects extending outside the scan field of view *Med.Phys.* **27** 39-46

Olson T and DeStafano J 1994 Wavelet localization of the Radon transform *IEEE Trans.Acoust.Speech Signal Process.* **42** 2055-2067

Pack J D, Noo F and Clackdoyle R 2005 Cone-beam reconstruction using the backprojection of locally filtered projections *IEEE Trans.Med.Imaging* **24** 70-85

Pan X, Zou Y and Xia D 2005 Image reconstruction in peripheral and central regions-of-interest and data redundancy *Med.Phys.* **32** 673-684

Pandy J N 1995 *The Hilbert Transform of Schwartz Distributions and Applications* (New York: Wiley Interscience)

Rullgard H 2004 An explicit inversion formula for the exponential Radon transform using data from 180° *Arkiv for Matematik* **42** 353-362

Stark H and Yang Y 1998 *Vector Space Projections: A Numerical Approach to Signal and Image Processing, Neural Nets and Optics* (New York: Wiley Interscience)

Tricomi F G 1957 *Integral Equations* (New York: Dover)

Ye Y, Yu H, Wei Y and Wang G 2007 A general local reconstruction approach based on a truncated Hilbert transform *Int.J.Biomed.Imaging* **2007** Article ID 63634

Ye Y, Zhao S, Yu H and Wang G 2005 A general exact reconstruction for cone-beam CT via backprojection-filtration *IEEE Trans.Med.Imaging* **24** 1190-1198

Youla D C and Webb H 1982 Image restoration by the method of alternating orthogonal projections: Part I. Theory *IEEE Trans.Med.Imaging* **1** 81-94

Yu L, Zou Y, Sidky E Y, Pelizzari C A, Munro P and Pan X 2006 Region of interest reconstruction from truncated data in circular cone-beam CT *IEEE Trans.Med.Imaging* **25** 869-881

Zhang B and Zeng G L 2007 Two-dimensional iterative region-of-interest (ROI) reconstruction from truncated projection data *Med.Phys.* **34** 935-944

Zhuang T, Leng S, Nett B E and Chen G-H 2004 Fan-beam and cone-beam image reconstruction via filtering the backprojection image of differentiated projection data *Phys.Med.Biol.* **49** 5489-5503

Zou Y and Pan X 2004 Exact image reconstruction on PI-lines from minimum data in helical cone-beam CT *Phys.Med.Biol.* **49** 941-959

Zou Y, Pan X and Sidky E Y 2005 Image reconstruction in regions-of-interest from truncated projections in a reduced fan-beam scan *Phys.Med.Biol.* **50** 13-27